Predicting the oxygen binding properties of platinum nanoparticle ensembles by combining high-precision electron microscopy & DFT

Journal:	*Nano Letters*
Manuscript ID	nl-2016-04799a.R4
Manuscript Type:	Communication
Date Submitted by the Author:	n/a
Complete List of Authors:	Aarons, Jolyon; University of Southampton, Chemistry Jones, Lewys; University of oxford, Department of Materials Varambhia, Aakash; University of oxford, Department of Materials MacArthur, Katherine; Ernst Ruska Center for Microscopy and Spectroscopy with Electrons, Forschungszentrum Jülich GmbH Ozkaya, Dogan; Johnson Matthey Technology Centre Sarwar, Misbah; Johnson Matthey Technology Centre Skylaris, Chris-Kriton; University of Southampton, Chemistry Nellist, Peter; University of Oxford, Materials

Predicting the oxygen binding properties of platinum nanoparticle ensembles by combining high-precision electron microscopy & DFT

Jolyon Aarons[1*], Lewys Jones[2*†], Aakash Varambhia[2*], Katherine E. MacArthur[3], Dogan Ozkaya[4], Misbah Sarwar[4], Chris-Kriton Skylaris[1], Peter D. Nellist[2]

1: School of Chemistry, University of Southampton, Highfield, SO17 1BJ, UK
2: Department of Materials, University of Oxford, Parks Road, OX1 3PH, UK
3: Ernst Ruska Center for Microscopy and Spectroscopy with Electrons, Forschungszentrum Jülich GmbH, 52425 Jülich, Germany
4: Johnson Matthey Technology Centre, Sonning Common, Reading, RG4 9NH, UK
[*] These authors contributed equally to this work.
[†] Corresponding author: lewys.jones@materials.ox.ac.uk

Abstract

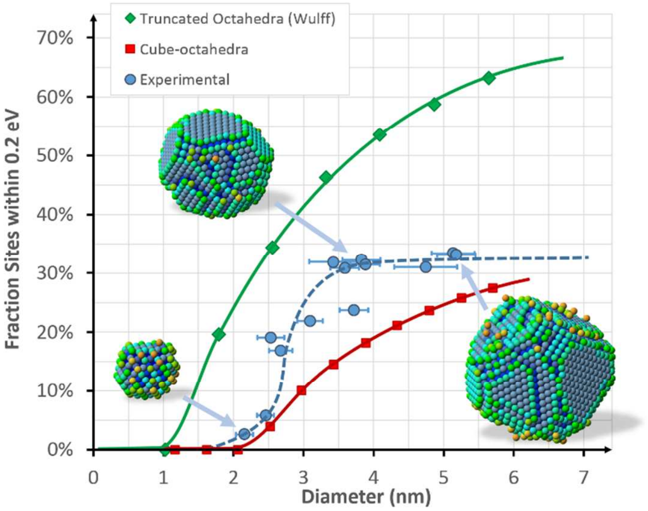

Many studies of heterogeneous catalysis, both experimental and computational, make use of idealised structures such as extended surfaces or regular polyhedral nanoparticles. This simplification neglects the morphological diversity in real commercial oxygen reduction reaction (ORR) catalysts used in fuel-cell cathodes. Here we introduce an approach that combines 3D nanoparticle structures obtained from high-throughput high-precision electron microscopy with density functional theory. Discrepancies between experimental observations and cuboctahedral/truncated-octahedral particles are revealed and discussed using a range of widely used descriptors, such as electron-density, d-band centres and generalized coordination numbers. We use this new approach to determine the optimum particle size for which both detrimental surface roughness and particle shape effects are minimised.

Keywords: heterogeneous catalysis, fuel cells, ADF STEM, density functional theory

When aiming to improve the function of heterogeneous catalysts, rapid characterisation of their morphological and chemical properties is required. Combining atomic resolution electron microscopy with electronic structure modelling can reveal new insights into catalyst function by enabling structure-property relationships to be determined. Both high-resolution electron microscopy and density functional theory (DFT) are each able to contribute very detailed insights right down to the atomic level; however, the applicability of both methods is often limited by the achievable throughput of measurements, the relatability between the two techniques, and the tendency for researchers to often study model systems.

Real catalyst systems show wide morphological variability, and it is necessary to characterise an ensemble of particles to understand and explain their overall activity. X-ray absorption fine structure (EXAFS) measurements can yield valuable insight into the coordination and chemical environments in materials [1]; and while there have been both impressive time-resolved [2] and spatially-resolved [3] studies on platinum and platinum-alloy fuel cell cathode materials, the nature of the broad-beam x-ray illumination means these are necessarily collective measurements and the action of individual nanoparticles is not considered. Here we use a high-throughput microscopy technique to determine the 3D structure of an ensemble of nanoparticles. Following that, a reduced-scaling DFT method is used to determine the electronic structure of a subset of the particles, enabling a widely applicable descriptor of oxygen binding-energy to be derived, and a prediction to be made of this binding across the entire ensemble of nanoparticles. We predict a size range with a binding-energy that most closely approaches the optimal case, and which is consistent with the current commercially optimised synthesis routes.

To enable the high-throughput structural characterisation, we use high-resolution annular dark-field scanning transmission electron microscopy (ADF-STEM). Obtaining atomic-resolution images of metallic nanoparticles is now routine in the aberration-corrected scanning transmission electron microscope (STEM). The annular dark-field imaging mode, with strong Z-contrast between the carbon support and the metallic nanoparticle [4], yields 2D projections (images) of the intrinsically 3D structures. Determining structures from such data then becomes an inversion problem. One possibility is electron tomography, though this requires generally very large electron doses or alternatively large, robust or embedded samples [5–8]. An alternative to tomography is to analyse the ADF image intensity [9,10], quantify the scattering cross-sections of atomic columns [11], and evaluate the number of atoms therein [12]. This cross-section approach is robust to sample tilt, source size, defocus, astigmatism and other aberrations in the electron probe [11,13,14], and as a dose-efficient alternative to tomography is a powerful tool when imaging real nanoparticles and not model systems.

Where larger fields of view are available, statistical parameterisation approaches can be used to interpret the cross-section measurements [15–17]. Here however, as the nanoparticles consist of relatively few atomic columns, we instead compare the image intensities against tabulated reference data to identify the numbers of atoms. These reference data are calculated via careful simulation, matched to all experimental parameters, for which we verify their overall accuracy through the master weighing curve (see Figure 1). By assuming particles are crystalline and contain no voids, the atom counts per column can be relaxed to yield 3D atomic structures through an empirical potential [12]. The ability to rapidly evaluate the atomic morphology of particles, without needing to tilt the sample to additional projections, unlocks a metrology regime with far higher throughput where whole ensembles of particles can be explored.

Similarly, DFT calculations have been widely and successfully used to study catalytic reactions on metallic surfaces [18–22]. However, with conventional DFT approaches, the computational burden scales with the number of atoms cubed. To endure this, many works have utilised periodic supercell approaches where only one type of crystal plane is modelled, or ultra-small so-called ‘magic number’ regular polyhedra. Unfortunately, these model structures exhibit only a small fraction of the diverse range of surface morphologies available for molecular interaction. The development of a new generation of linear-scaling methods (such as the ONETEP program [23] via which DFT calculations on larger systems can be performed [24]) has brought catalytically relevant sizes of nanoparticles (2-10nm) into reach.

The major challenge in developing linear-scaling DFT approaches is being able to retain the same high level of accuracy as conventional cubic-scaling DFT. DFT calculations for metallic systems are more challenging than those for insulators and the development of reduced-scaling, or even linear-scaling methods, for metallic systems is an open area of research [25]. While a linear-scaling DFT method for metals is not yet available, there has been significant progress in the development of reduced-scaling DFT methods for large-scale calculations on metallic systems. The DFT method implemented in the ONETEP program offers the capability of performing DFT calculations on metallic systems with several thousand atoms [26]. By modelling both ideal and experimental nanoparticles, the degree of deviation between the two regimes can be understood, particularly with respect to the interaction of adsorbates with the nanoparticle surface.

Many previous studies have focussed on ideally shaped nanoparticles such as those based on cuboctahedra or icosahedra [27–29]. Experimental nanoparticles are likely to deviate from these “ideal” shapes and this introduces the risk of discrepancies arising between predictions made from DFT calculations and experimental results. As a test case we take the oxygen reduction reaction (ORR), which takes place at the cathode of proton exchange membrane (PEM) fuel cells, and model the binding-energies of atomic oxygen on both perfect cuboctahedra and experimentally observed nanoparticles. According to the Sabatier principle, catalytic activity is controlled by the binding strength of reactive intermediates [18]; in the case of the ORR, these are oxygen and hydroxyl bound to the metal surface. An optimal catalyst should not bind O_2 too weakly, thus preventing the molecule from dissociating, nor should it bind the intermediates O and OH too strongly, smothering the surface, blocking active sites, and preventing the reaction from proceeding further. Thus binding-energies of reactants to nanoparticle surfaces have been used as a descriptor for catalytic activity in many studies which also seek to understand how this is affected by particle size [28]. Previous estimates for the optimal binding-energies vary slightly depending on the precise DFT computations performed and extrapolations made, but have been quoted as 0.2eV weaker [18,30], or 0.25eV weaker [31] than for that of the Pt(111) surface.

The sample investigated here was taken from a commercially produced ORR catalyst system consisting of Pt nanoparticles on a carbon-black support. In order to contextualise the subsequent ensemble of atomic models, we first evaluate the wider particle size distribution. ADF STEM images were recorded using a JEOL3000F equipped with a Fischione 3000 ADF detector (further experimental particulars are discussed in the supplement).

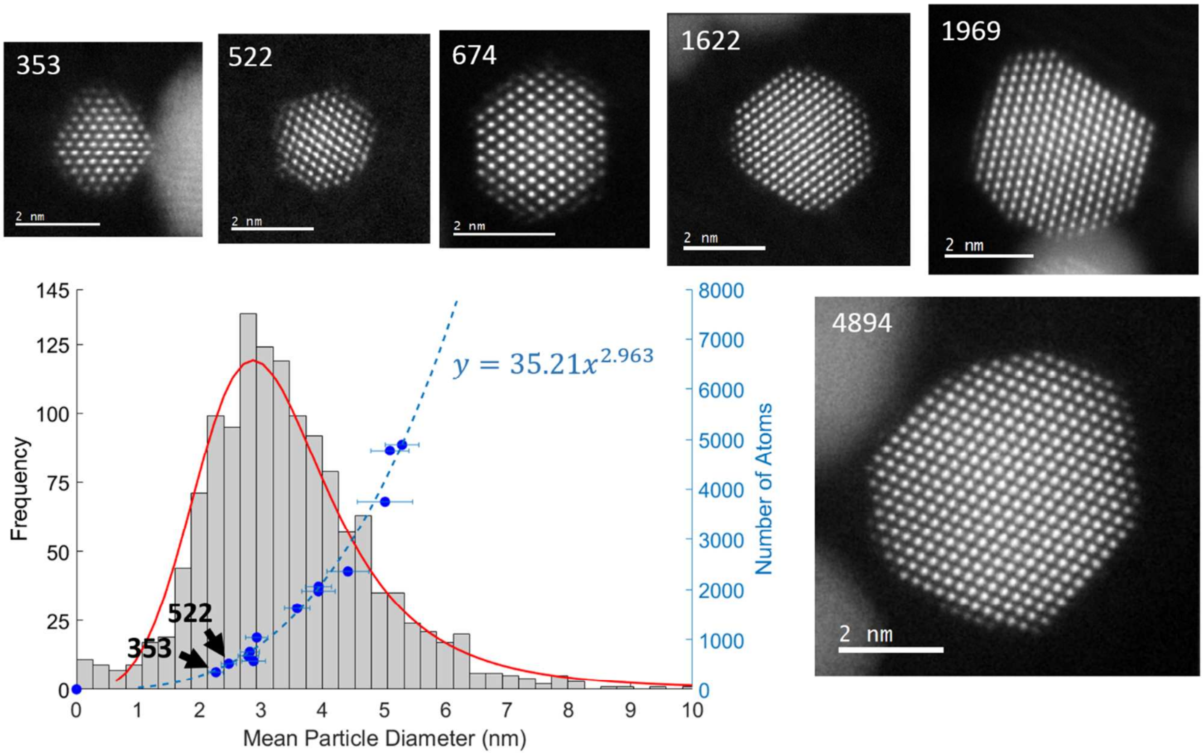

Figure 1. Particle size distribution calculated from 1342 observations (mean diameter 3.46nm, median: 3.25nm) with representative HR-STEM images labelled by total atom count. The overlaid scatter plot (blue points) shows the measured number of atoms (right axis) as a function of particle diameter. The particles with 353 and 522 atoms are shown and their relative positions in the population histogram are highlighted.

A histogram of the distribution of nanoparticle sizes is shown in Figure 1, from 1342 observations a mean particle size of 3.46 nm was determined. In addition to the size histogram, high-resolution (HR) STEM images were recorded over as wider size range as possible using a JEOL ARM200CF fitted with a probe-aberration corrector. Care was taken to minimise sources of experimental error from detector or column misalignment [32]. Following the experiment design optimisation of DeBacker et al. [33], a relatively long camera-length of 12 cm was selected yielding an ADF collection angle of 51.7-248.4mrad. To minimise sample damage and to correct for non-linear scanning-distortions, a series of images were recorded in quick succession [34]; linear scan-drift was also minimised by incorporating a 90° scan-rotation between successive frames [35]. Electron dose was evaluated at $1.38\ 10^{4}\ e^{-}Å^{-2}$ per frame which, for a typical series of 20 frames, becomes $2.76\ 10^{5}\ e^{-}Å^{-2}$ after integration. This is above the minimum dose shown to be necessary to achieve single atom counting sensitivity [36]. An example of frames from the time-series acquisition are shown in the supplementary information. From the time-series, we can observe when an atom-hopping event has taken place (an indicator of damage) and can choose how many frames from the start of the series to integrate. This ‘post-mortem’ style of analysis allows us to find the ideal optimum between integrating more frames to improve signal-noise ratio (SNR) but without introducing artefacts from beam-damage. Even though every care was taken to minimise beam-damage, we were unable to record atomic resolution on-axis images of particles below 2nm diameter.

Of the many particles imaged 13 were sufficiently close to a zone axis to allow accurate atom counting and a representative selection of these from across the size range are also shown inset in Figure 1. Further ADF images are shown in Figure 2; already we see qualitatively that there is a variety of shapes even for particles of similar size.

Atom-counts from the high-resolution frames are plotted as a function of particle diameter, where the fit follows a cubic relation as expected. The measured pre-factor of 35.21 is within a 0.2% agreement with the value of 35.25 expected for a bulk-like number density of Pt atoms [37] (see supplementary information for derivation). This confirms that the overall ‘nano-weighing’ of each particle is accurate, giving then a good confidence in the *accuracy* of the atom-count assignments for each atomic column in the HR-STEM images. The *precision* of these assignments is dictated by other factors including sample-tilt, scan-distortion [34] and Poisson noise [36], though every effort was made to minimise these.

From these images, the number of atoms in each individual atomic column were counted, and 3D reconstructions produced based on the energy minimisation method described in Jones et al. [12,38]. A genetic algorithm was used to search as wide as possible energy landscape; this is based on the work of Yu et al, but using the experimental atom-count data rather than computationally expensive full-field image matching [39]. This energy minimisation provides a computationally efficient but somewhat simplified approach to determining the optimum structure for each particle; as a result, these were followed by a more computationally intensive and fully unconstrained geometry relaxation performed using the Sutton-Chen force field within the DL_POLY4 software [40]. During this relaxation, a small relaxation of the atomic separations was observed around the periphery of the particles (RMS differences between the initial and final structure of 0.1 Å).

Of the particles observed, some contain a number of atoms close to a ‘magic number’ of atoms of truncated cuboctahedra commonly used in DFT studies (Figure 2); ball models of all the experimentally observed structures are shown in the supplement.

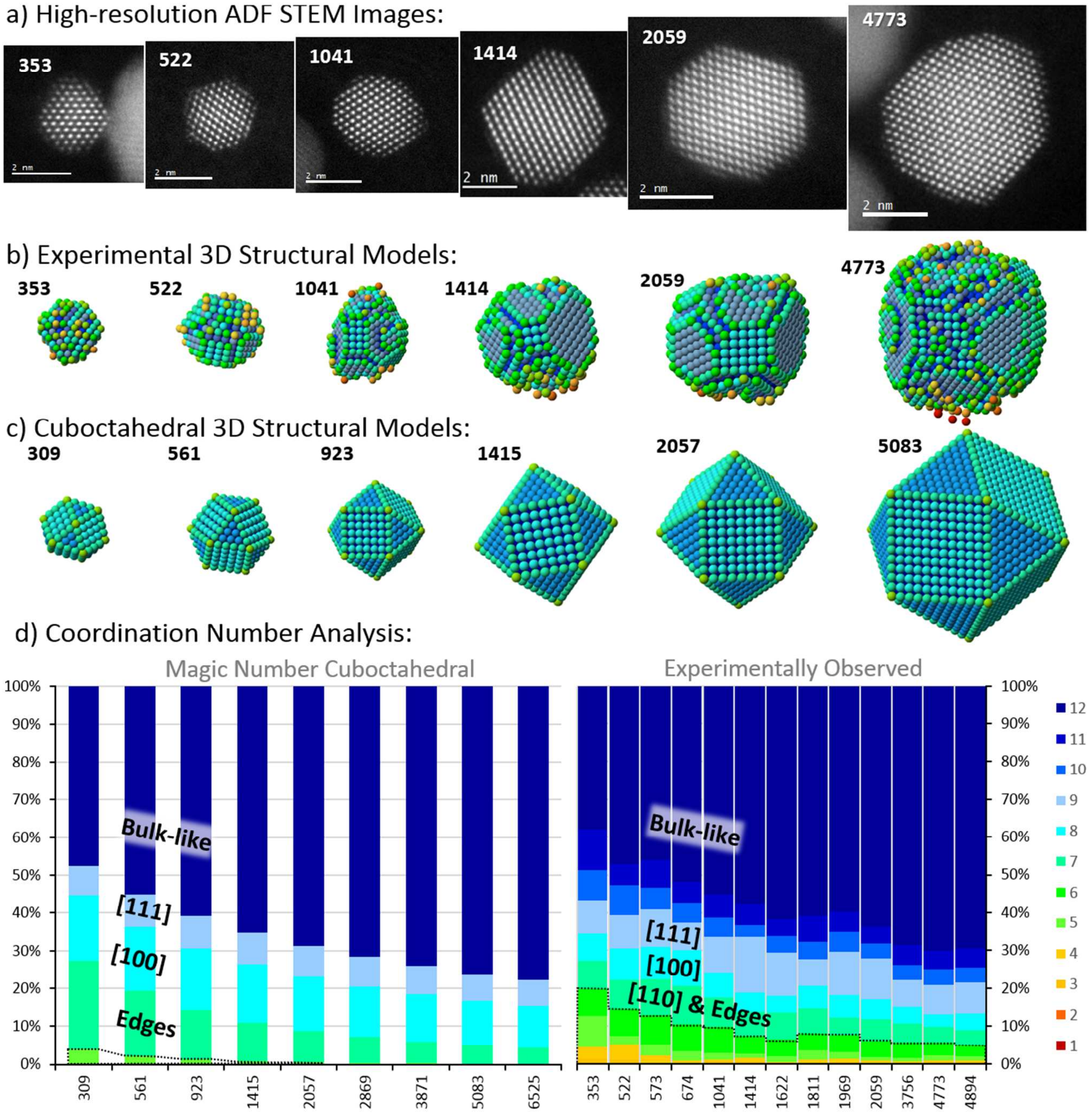

Figure 2. HR-STEM images (a) and accompanying hard-sphere models (b) for experimental particles observed with atom-counts near to magic-numbers; models are coloured by atom coordination numbers [12] *and rotated to show their dominant facets. Magic number cuboctahedra are shown for comparison rotated to the same orientations (c). Population histograms (d) show the coordination number fractions as a function of particle atom-count for both magic (left) and experimentally observed particles (right). The 7, 8, and 9 coordination atoms corresponding loosely to both (110)*

facets and edges between facets, and (100) and (111) surfaces respectively are labelled, as well as the 'bulk-like' atoms of ≥10 coordination. The dashed area represents the fraction of low-coordination adatom, corner and step sites.

The coordination number information from Figure 2 reveals some important results. Firstly, as particle size increases the proportion of bulk-like coordinations (≥10 coordination) increases; a classic surface area to volume effect. Secondly, all the experimental particles observed showed some surface roughness with significantly more atoms of lower coordination than cuboctahedral nanoparticles of equivalent size. The dashed area in Figure 2 represents the low-coordination sites (6 and fewer) and this is 20% of the *total* atoms in the 353 atom particle, rising to more than 46% if we consider these as a proportion of the *surface* atoms.

Owing to the computational demands of DFT, only the two smallest experimental models containing 353 and 522 atoms were used for DFT calculations, as well as the cuboctahedral nanoparticles with 309 and 561 atoms which are of similar size to these two experimental nanoparticles. These required significant supercomputer resources, and so particles larger than this (> 2.8 nm diameter) were not studied here with DFT. Electronic calculations were performed with the ensemble-DFT method [26] for metallic systems in the ONETEP linear-scaling DFT program [23]. The Revised Perdew-Burke-Ernzerhof (RPBE) exchange correlation functional was used [41] (further details of the computational methodology can be found in the supplementary Information).

Although only two cuboctahedral, and two experimental structures were computed, our aim is to obtain descriptive information from the DFT calculations which can be used to predict chemical properties across the observed ensemble of nanoparticles. To achieve this, we first map the local electronic-density calculated on an isosurface of the total electrostatic potential of the nanoparticle (0.0 E_h has been used throughout this work). Figure 3 shows these maps for the two smallest experimental particles and their closest magic number analogues.

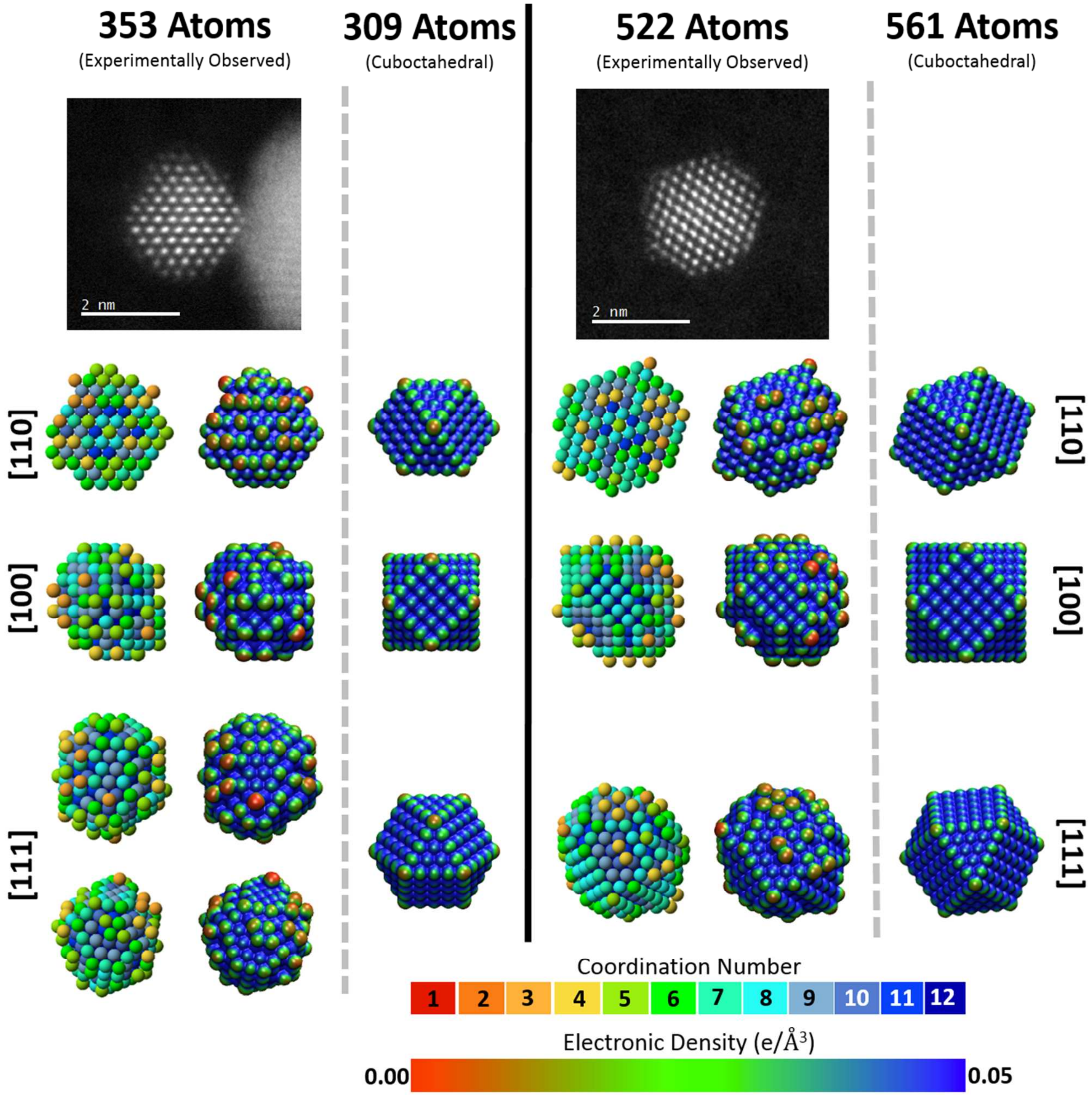

Figure 3. Coordination number and DFT analyses for the smaller (left) and larger (right) nanoparticles studied. Hard-sphere structural models were calculated from the ADF data and are coloured according to their coordination number; these are shown rotated to various viewing directions to highlight their morphology. Alongside the structural models, the DFT results showing isovalue surfaces of total electrostatic potential at 0.0 Ha colourised by the local electronic-density. Size analogue cuboctahedra DFT results are shown for comparison.

By comparing the electronic charge density maps between the experimentally measured and cuboctahedral nanoparticles, it is immediately apparent that the experimental structures show a far greater number of sites of low electron-density compared to their cuboctahedral counterparts.

Atoms with lower coordination numbers exhibit lower electron-density values on their surfaces (as sampled on the electrostatic isosurface) due to the well-known Smoluchowski effect [42]. This effect describes the observed [43–45] spreading out of electronic charge density at sharp, surface corrugations and defects resulting in loss of electron-density above low coordinated sites (see supplementary information Figure S6). This is particularly visible when contrasting the relatively high electronic charge density on facets of the cuboctahedral nanoparticles with the lower density values on the edges and even more electron deficient vertices. Also, when examining the experimental particles, very high-density sites are visible under vacancy defects [46], where the atomic centre has high coordination number, and very electron deficient isosurface sites can be seen on adatoms with low coordination number.

The results from the electronic charge map descriptor are compared with the other descriptors we have investigated, namely oxygen binding-energies at various sites (which can be directly related to catalytic activity), the d-band centres [47] (see supplementary information), and partitioning of electronic charge on atoms.

The electronic-density iso-surfaces also highlight a greatly different diversity of surface sites between the magic-number and experimental models. To evaluate this systematically an algorithm was developed to identify all the possible atop, bridge, and hollow sites across the surface of the nanoparticles and implemented into a stand-alone program (this can be found in the ‘Utilities’ section at www.onetep.org). The results of this are illustrated for the Pt_{309} model in the supplementary information. Using this code, the generalized coordination number (gCN) of every possible site for an oxygen adsorbate was calculated (using the formula from Calle-Vallejo et al. [48]) for every one of the experimental and magic-number atomistic models. The results for the three smallest nanoparticles are shown in Figure 4.

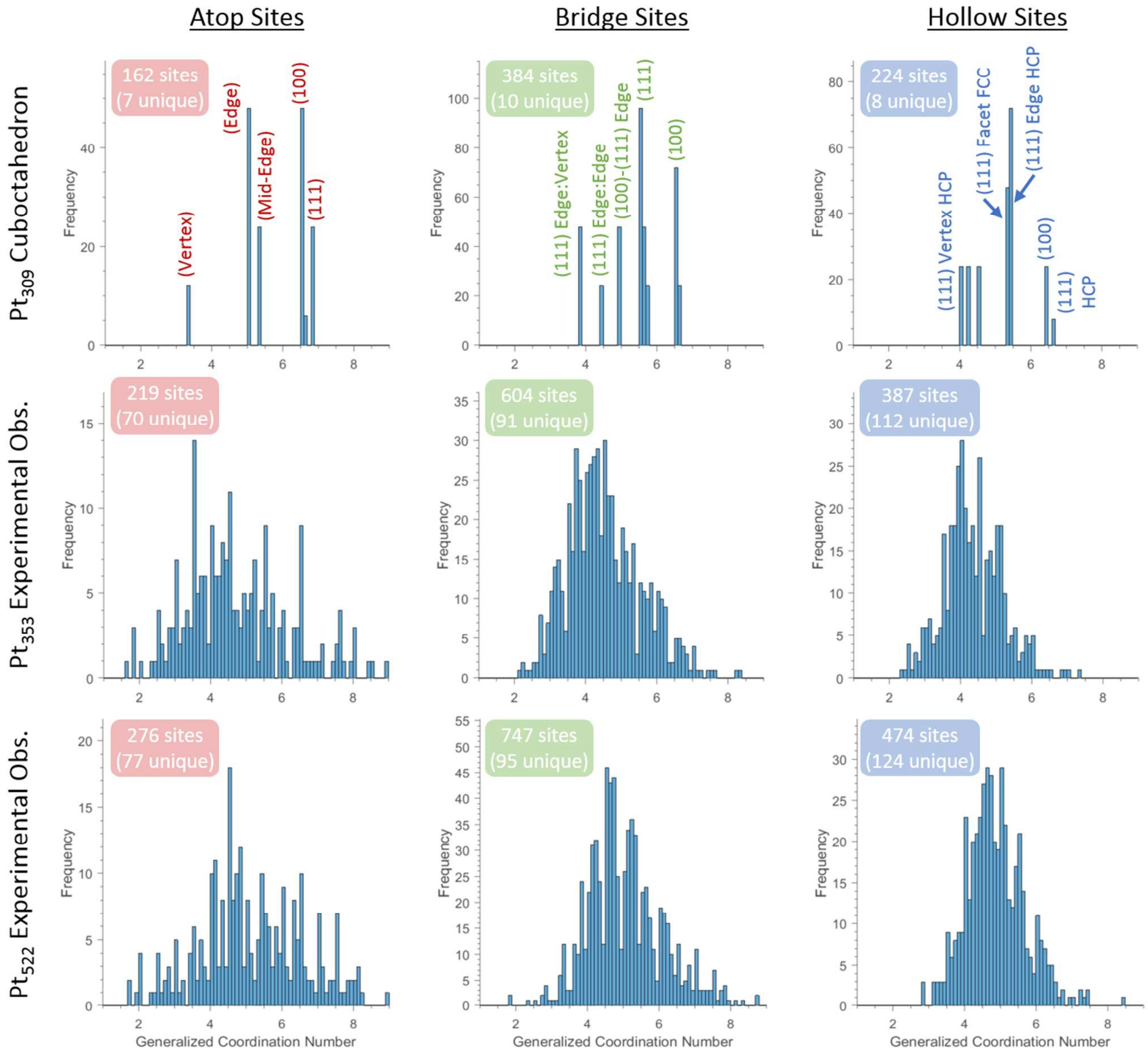

Figure 4. Histograms of the generalized coordination numbers of all possible surface atop, bridge and hollow oxygen binding sites, for the cuboctahedral Pt_{309} and the experimental Pt_{353} and Pt_{522} particles. For all plots, the number of total sites are indicated and the number of unique sites.

The histograms in Figure 4 reveal several insightful features. Firstly as expected, the magic-number Pt_{309} exhibits only a small number of unique gCN oxygen binding sites; a total of 25 unique-sites describe every possible symmetry-related adsorption site, and a systematic DFT study is relatively tractable. For the experimental Pt_{353} of similar size, the surface roughness leads to a far greater number of unique site-geometries, 273 unique sites in total. The largest of the experimental models in this work exhibits ≈8300 surface adsorption sites with 539 unique geometries. From these histograms, the experimentalist may mine the data in various ways depending on their onward investigation; for example, though not done here, one can easily extract ‘the fraction of hollow-sites out of all sites’ or ‘the number of total oxygen-binding sites with a gCN greater than 8’, plotting each as a function of particle size. Instead here, with this collection of models of increasing size and of adsorption site diversity, we are no longer seeking to study each of the many thousand unique adsorption sites, but rather to extract some single parameter to compare nanoparticles across the ensemble.

While the colour-coded iso-surface representations provide a visual qualitative descriptor of the strength of O binding, quantitative values can also be extracted across the ensemble of nanoparticles measured. Figure 5 shows the oxygen binding-energies across a variety of sites from a Pt_{309} cuboctahedron and also single-crystal slab models (as computed by DFT calculations) both as a function of the electron-density value on the potential isosurface, and as a function of their generalized coordination number [48]. Further models for the adatom variants used for the calculations leading to Figure 5 are shown in the supplementary information (Figure S6). Electronic-density values, for each binding site (whether atop, bridge, or hollow) are used as descriptors of O binding strength, providing linear relationships for each binding-energy as a function of electron-density value. Information about how these values are extracted, for each type of site (atop, bridge or hollow), is provided in the supporting information. One advantage of such electronic descriptors is that they are expected to apply also to alloyed nanoparticles, or particles with inbuilt surface strains, which we intend to explore in a future work.

The DFT O adsorption energies were computed according to the following equation:

$$E_{bind} = E_{NP+O} - E_{NP} - \frac{1}{2}E_{O_2}$$

where E_{NP} is the total energy of the bare, clean nanoparticle in vacuum fully relaxed by DFT, E_{NP+O} is the total energy of the nanoparticle with a single oxygen atom adsorbed onto the test site, and E_{O_2} is the total energy of an oxygen molecule in isolation fully relaxed by DFT. To maximise the throughput of unique sites evaluated in a reasonable computation time, the Pt positions in the nanoparticle are kept fixed in their vacuum optimised geometries while each O atom is fully relaxed. To validate this approximation, results were compared with slabs using full relaxation. In these calculations, the degrees of freedom of all atoms in the three surface layers were free to relax due to the presence of the oxygen, along with the oxygen degrees of freedom. The bottom two layers remained constrained to be bulk-like. The change in oxygen binding strength, observed when allowing the platinum atoms to relax due to the presence of the oxygen (Figure 5, black diamonds), is consistently a stronger binding by ≈0.2 eV. As we are aiming for a high throughput analysis, calculating the effect of the Pt relaxation for all sites is not feasible. Rather than opting to apply a uniform 0.2 eV strengthening to the binding energy for all sites, it is simpler here to recognise that we are primarily interested in the relative differences in energy between sites, and therefore use the binding energies without Pt relaxation. Results from the cuboctahedra and the slab calculations are shown together in Figure 5.

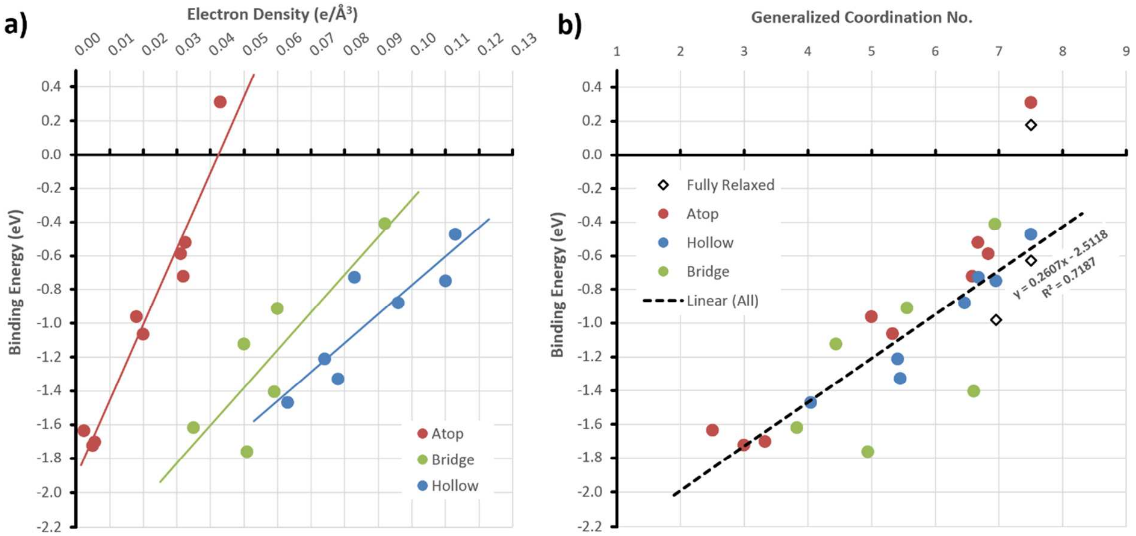

Figure 5. Calculated oxygen binding-energies for various oxygen-relaxed atop, bridge and hollow sites from both a cuboctahedral Pt_{309} nanoparticle, and from slab calculations, as a function of electron-density (a) and gCN (b). The gCN values are calculated using the formula from Calle-Vallejo et al.[48]*. Black diamonds represent the results of fully-relaxed (oxygen and platinum) calculations.*

Binding-energy calculations for oxygen at various sites (Figure 5a)) shows that oxygen binds most strongly to sites predicted to have low electron densities. Similarly (shown in the supplement), surface atom d-projected DOS, resolved according to the coordination number of surface atoms shows that reducing the coordination number shifts the d-band centre to higher (more positive) values. This is in accordance with the d-band model of Nørskov [20] which suggests enhancements of binding strength as the d-band centre becomes more positive. From our calculations the $Pt_{(111)}$ binding-energy (at a hollow FCC site on a slab without Pt relaxation) was found to be -0.751eV.

Previous literature [18,30,31] suggests that the optimal binding energy is ≈0.22eV weaker than the binding energy for the $Pt_{(111)}$ hollow-site. Using our energies calculated with unrelaxed Pt, this would suggest an optimal binding energy of -0.53eV.

Atop sites are only found to be energetically favoured (most negative) for gCNs lower than ≈3.5. At higher coordination, the bridge and then hollow sites are expected to dominate. Unlike the simple geometric coordination numbers of the metal atoms shown in Figure 2 & Figure 3, the generalized coordination number of the oxygen-adsorbate sites (Figure 4 & Figure 5) capture a more subtle weighted average of the neighbouring atoms. The quality of the generalized coordination number as a descriptor of oxygen binding-energy has been shown to offer a powerful tool for catalyst evaluation [27,46,48,49], and has been exploited in the engineering of defective extended surfaces, but not so far for nanoparticles [46]. The approach has also already been reported to yield reliable results across different sizes of metallic nanoparticles [46,48].

From the data in Figure 5 b) we fit a linear trend which allows us to extrapolate from the individual, and computationally expensive, DFT calculations and onto the many thousand unique sites across the experimental observations, and predict a binding-energy for every surface site. So-called “volcano plots” that follow from the Sabatier principle of catalyst activity, whether from different materials [18,50] or for platinum surface sites of different coordinations [46], show that pure platinum surfaces always bind oxygen slightly too strongly (desorption limited). At present is it not computationally practicable to calculate the chemical-activity of every site across the particle surface. Here, as a useful metric of overall particle catalytic activity, we consider the fraction of surface sites within 0.2 eV of the optimum binding strength of -0.52 eV, and this fraction can be rapidly calculated using the linear fit in Figure 5 b). While this may not explicitly yield a quantitative relationship to chemical-activity, it does offer a rapidly calculated metric for comparing any given particle with reference to the rest of the ensemble. This ‘fraction of sites within 0.2eV’ ($F_{\Delta<0.2eV}$) metric is more subtle than simply counting the fraction of {111} sites, is sensitive to particle-size, shape and roughness, and so can be used to evaluate the comparative catalytic performance of nanoparticles from a real catalyst sample.

To summarise; from high-quality ADF images and computationally efficient relaxations, we have the 3D locations of the metal atoms, the locations of all possible oxygen binding sites, and the generalized coordination numbers of all those sites. Combining this with the DFT master-trend from Figure 5 b), we are able to calculate a $F_{\Delta<0.2eV}$ for each observed particle. This site-identification and master-trend scaling is rapidly calculated, even for very large particles, and is shown in Figure 6 for both the experimental particles and for thermodynamically predicted Wulff shapes (truncated cuboctahedra), for cuboctahedra and quasi-spherical comparators.

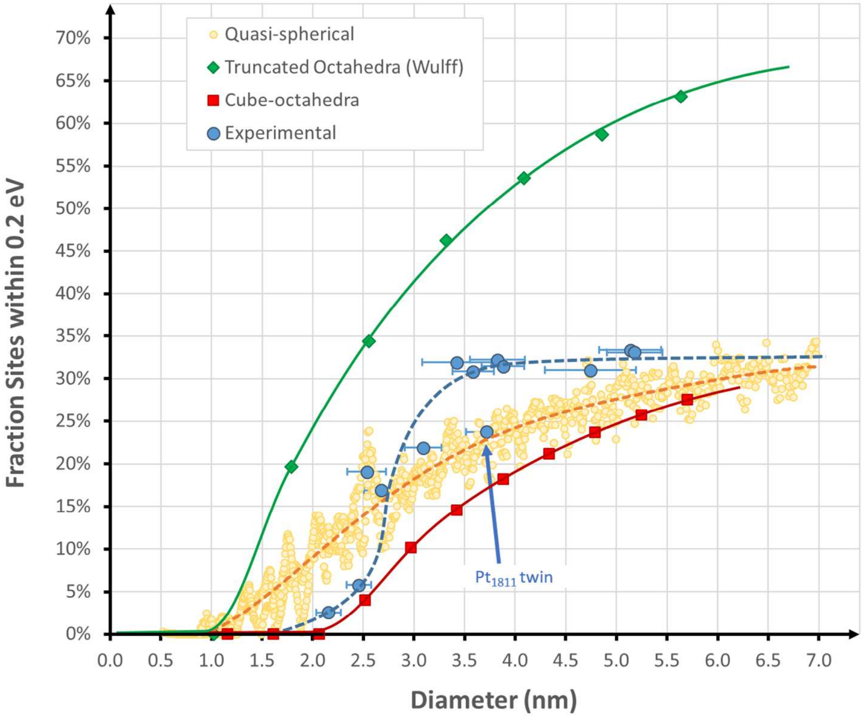

Figure 6. Fraction of surface sites within 0.2eV of optimal binding ($F_{\Delta<0.2eV}$) for the 13 experimentally observed particles, and truncated-octahedra, cube-octahedra and quasi-spherical reference particles.

For the Wulff-shape magic-number particles we see a monotonic curve dominated by simple size effects. Even though, by definition, all the models following a Wulff shape series have similar {111}/{100} face area ratios, at small diameters the excess of low coordinated edges and vertices results in a smaller $F_{\Delta<0.2eV}$. This $F_{\Delta<0.2eV}$ falls to zero for truncated-octahedra below 1.5 nm and is consistent with the data reported by Shao et al. for their particles smaller than 2nm [28]. Experimentally we were unable to observe particles smaller than 2nm on-axis in the HR-STEM; in addition to these being only a small number-fraction of all present, even when found these are highly sensitive under the electron beam. A similar trend is observed in the cube-octahedral series, though with the sharper tips of such models yielding very low-coordination sites, the $F_{\Delta<0.2eV}$ falls to zero for all models below 2.0 nm.

The $F_{\Delta<0.2eV}$ for the experimentally observed particles was found to always be lower than for the Wulff shapes but higher than the cube-octaherda. That is to say that the experimental results are all bounded by one of these two geometric models. From this we might conclude, that while it is generally valid to use perfect-model geometric-series for simplified surface studies, the true experimental surface will always reveal more subtle details. From the structural models (Figure 2 & supplementary info.), and the gCN histogram analysis (Figure 4) we observe both an increase in roughness compared with Wulff shapes, and also a general lowering of the surface gCN. Because the lowest coordination sites are so strongly over-bound, rough adatom sites effectively poison the surface locally blocking otherwise high-coordination sites below. The downward shift of the experimental curve from the Wulff trend for the largest and smallest particles encompass the various topographic-effects, reducing the $F_{\Delta<0.2eV}$ for these models. In contrary, relative to the cube-octahedral models, we see the opposite effect where $F_{\Delta<0.2eV}$ is now improved in comparison to the perfect models (consistent with the increased fraction of {111} facets observed). Both these relative results indicate that caution must be exercised when comparing experimental chemical activity measurements to geometric simulations, something we hope to study in a future work.

As a further comparison, a series of 1600 randomly generated single-crystal quasi-spherical models were also generated and the $F_{\Delta<0.2eV}$ evaluated. These models were formed from a single-crystal lattice with only atoms within a radius threshold from the origin kept; this radius was stepped larger to create all the model in the series. Because of the discrete atomic nature of the spherical models, the surfaces are not perfectly smooth but rather a mixture of small facets and rougher high-index sites.

The $F_{\Delta<0.2eV}$ reaches most closely to the Wulff trend for particles in the size range of 2.7-3.5nm; with these models (with their increase fraction of {111} facets) sitting higher than the quasi-spherical trend but still falling short of the Wulff models. The location of this optimum is consistent with the industrially optimised synthesis process (determined from trial and improvement), and the specific-activity observations previously reported [28]. For the very largest experimentally determined nanoparticle structures, these appear more spherical, suggesting that they are further from their thermodynamic optimum shape and their shape is more kinetically limited, and indeed the $F_{\Delta<0.2eV}$ approaches the quasi-spherical trend. From inspection of Supplementary Figure S4, it can be seen that the larger particles do not show a commensurate increase in {111} facet area and have become more spherical.

Two twinned particles were observed at 3.7nm (1811 atoms) and at 3.8nm (1969 atoms). While one of these was well below the wider trend, as only two of the thirteen particles in this study contained twins, a wider study of twinned particles would be required before making any specific conclusions about these. Finally, the cube-octahedral series of particles show the lowest $F_{\Delta<0.2eV}$ of any series, and underestimate the $F_{\Delta<0.2eV}$ at 3.5 nm compared to the experimental result by the same amount that Wullf-shapes overestimate this. Figure 6 then highlights two important points; firstly presumptive model geometries alone should not be relied upon when studying expected chemical behaviours, and secondly, that if they are then catalyst synthesis optimisation can be misinformed.

In conclusion, the three-dimensional structural models presented here, with up to 5000 atoms each, can each be calculated from experimental data in only a few hours on a standard desktop computer [12]. These structural models can be used as inputs to reduced-scaling DFT calculations to yield the electronic structure of the experimental nanoparticles. It is observed that increased roughness, compared to the equilibrium Wulff structures, lead to more sites with lower electron-density and therefore higher O-binding reducing activity. Using a DFT-generated binding-energy master-trend calibration plot, an estimate for the ‘fraction of sites within 0.2eV’ ($F_{\Delta<0.2eV}$) can be calculated in only a few seconds for an ensemble of experimentally determined structures. This would be computationally unfeasible to do by DFT calculation of individual adsorption energies for each of the sites of each nanoparticle. By leveraging the accuracy of large-scale DFT calculations on small models, via the generalized coordination calibration relation, we can gain insight into a far wider ensemble of atomic models than would otherwise be possible. This high-throughput approach agrees well with other reported experimental [28,50] and simulated [49] findings for this system and offers the potential to accelerate the development of better tuned catalysts for the ORR. Similar calibrations for other species have been reported and may lead to the optimisation of other systems [51]. In this work, the generalized coordination descriptors were evaluated for pure metal nanoparticles. While these may not be expected to be simply transferable to doped or alloyed cases, the electronic descriptors can be; these come at an increased computational cost with a single point energy calculation needed for each nanoparticle structure that needs to be studied but are nevertheless dramatically less demanding than having to do a DFT calculation of adsorption energy for each distinct site. In the future, the $F_{\Delta<0.2eV}$ metric seems well suited to future extension from gCN to electronic-density, exploiting other experimental inputs, such as changes in binding-energy arising from composition [18] or atomic displacement (strains) [47]. The current rapid pace of progress in experimentally mapping composition and strain in the STEM merits revisiting this concept in the near future.

Supporting Information Available

Supporting information is available showing further experimental particulars, an example of the frames from an experimental time-series, details of the DFT calculations, and d-band structures for the truncated-octahedron and experimental particles.

Acknowledgements

The experimental work was carried on JEOLARM200CF at the University of Oxford which was funded by the EPSRC (grant: EP/K040375/1 - 'South of England Analytical Electron Microscope'). The calculations for this work were carried out on the Iridis4 Supercomputer of the University of Southampton and the ARCHER supercomputer via the UKCP consortium (EPSRC grant: EP/K013556/1). JA, AV and KEM acknowledge the EPSRC and Johnson-Matthey for PhD funding. The research leading to these results has received funding from the European Union Seventh Framework Programme under Grant Agreement 312483 - ESTEEM2 (Integrated Infrastructure Initiative–I3). Note: the authors declare no competing financial interest.

References

(1) Price, S. W. T.; Zonias, N.; Skylaris, C. K.; Hyde, T. I.; Ravel, B.; Russell, A. E. *Phys. Rev. B - Condens. Matter Mater. Phys.* **2012**, *85* (7), 75439.

(2) Ishiguro, N.; Saida, T.; Uruga, T.; Nagamatsu, S.; Sekizawa, O.; Nitta, K.; Yamamoto, T.; Ohkoshi, S.; Iwasawa, Y.; Yokoyama, T.; Tada, M. *ACS Catal.* **2012**, *2* (7), 1319–1330.

(3) Takao, S.; Sekizawa, O.; Nagamatsu, S.; Kaneko, T.; Yamamoto, T.; Samjeské, G.; Higashi, K.; Nagasawa, K.; Tsuji, T.; Suzuki, M.; Kawamura, N.; Mizumaki, M.; Uruga, T.; Iwasawa, Y. *Angew. Chemie Int. Ed.* **2014**, *53* (51), 14110–14114.

(4) Nellist, P. D.; Pennycook, S. J. *Science (80-.).* **1996**, *274* (5286), 413–415.

(5) Batenburg, K. J.; Sijbers, J. *IEEE Trans. Image Process.* **2011**, *20* (9), 2542–2553.

(6) Goris, B.; Roelandts, T.; Batenburg, K. J.; Heidari Mezerji, H.; Bals, S. *Ultramicroscopy* **2013**, *127*, 40–47.

(7) Van Aert, S.; Batenburg, K. J.; Rossell, M. D.; Erni, R.; Van Tendeloo, G. *Nature* **2011**, *470* (7334), 374–377.

(8) Bals, S.; Casavola, M.; van Huis, M. A.; Van Aert, S.; Batenburg, K. J.; Van Tendeloo, G.; Vanmaekelbergh, D. *Nano Lett.* **2011**, *11* (8), 3420–3424.

(9) LeBeau, J. M.; Findlay, S. D.; Allen, L. J.; Stemmer, S. *Phys. Rev. Lett.* **2008**, *100* (20), 206101-.

(10) LeBeau, J. M.; Findlay, S. D.; Allen, L. J.; Stemmer, S. *Nano Lett.* **2010**, *10* (11), 4405–4408.

(11) E, H.; MacArthur, K. E. K. E.; Pennycook, T. J. T. J.; Okunishi, E.; D'Alfonso, A. J. J.; Lugg, N. R. R.; Allen, L. J.; Nellist, P. D. P. D. *Ultramicroscopy* **2013**, *133*, 109–119.

(12) Jones, L.; MacArthur, K. E.; Fauske, V. T.; van Helvoort, A. T. J.; Nellist, P. D. *Nano Lett.* **2014**, *14* (11), 6336–6341.

(13) Martinez, G. T. G. T.; De Backer, A.; Rosenauer, A.; Verbeeck, J.; Van Aert, S. *Micron* **2013**, *63*, 57–63.

(14) MacArthur, K. E.; D'Alfonso, A. J.; Ozkaya, D.; Allen, L. J.; Nellist, P. D. *Ultramicroscopy* **2015**, *156*, 1–8.

(15) den Dekker, A. J.; Van Aert, S.; van den Bos, A.; Van Dyck, D. *Ultramicroscopy* **2005**, *104* (2), 83–106.

(16) Aert, S. Van; Verbeeck, J.; Erni, R.; Bals, S.; Van Aert, S.; Luysberg, M.; Dyck, D. Van; Tendeloo, G. Van. *Ultramicroscopy* **2009**, *109* (10), 1236–1244.

(17) De Backer, A.; Martinez, G. T. G. T.; Rosenauer, A.; Van Aert, S. *Ultramicroscopy* **2013**, *134*, 23–33.

(18) Stamenkovic, V.; Mun, B. S.; Mayrhofer, K. J. J.; Ross, P. N.; Markovic, N. M.; Rossmeisl, J.; Greeley, J.; Nørskov, J. K. *Angew. Chemie Int. Ed.* **2006**, *45* (18), 2897–2901.

(19) Mavrikakis, M.; Hammer, B.; Nørskov, J. K. *Phys. Rev. Lett.* **1998**, *81* (13), 2819–2822.

(20) Nørskov, J. K.; Bligaard, T.; Rossmeisl, J.; Christensen, C. H. *Nat. Chem.* **2009**, *1* (1), 37–46.

(21) Stephens, I. E. L.; Bondarenko, A. S.; Perez-Alonso, F. J.; Calle-Vallejo, F.; Bech, L.; Johansson, T. P.; Jepsen, A. K.; Frydendal, R.; Knudsen, B. P.; Rossmeisl, J.; Chorkendorff, I. *J. Am. Chem. Soc.* **2011**, *133* (14), 5485–5491.

(22) Viñes, F.; Gomes, J. R. B.; Illas, F. *Chem. Soc. Rev.* **2014**, *43* (14), 4922.

(23) Skylaris, C.-K.; Haynes, P. D.; Mostofi, A. A.; Payne, M. C. *J. Chem. Phys.* **2005**, *122* (8), 84119.

(24) Wilkinson, K. A.; Hine, N. D. M.; Skylaris, C.-K. *J. Chem. Theory Comput.* **2014**, *10* (11), 4782–4794.

(25) Aarons, J.; Sarwar, M.; Thompsett, D.; Skylaris, C.-K. *J. Chem. Phys.* **2016**, *145* (22), 220901.

(26) Ruiz-Serrano, A.; Skylaris, C.-K. *J. Chem. Phys.* **2013**, *139* (5), 54107.

(27) Han, B. C.; Miranda, C. R.; Ceder, G. *Phys. Rev. B - Condens. Matter Mater. Phys.* **2008**, *77* (7), 75410.

(28) Shao, M.; Peles, A.; Shoemaker, K. *Nano Lett.* **2011**, *11* (9), 3714–3719.

(29) Dobrin, S. *Phys. Chem. Chem. Phys.* **2012**, *14* (35), 12122.

(30) Greeley, J.; Stephens, I. E. L.; Bondarenko, A. S.; Johansson, T. P.; Hansen, H. A.; Jaramillo, T. F.; Rossmeisl, J.; Chorkendorff, I.; Nørskov, J. K. *Nat. Chem.* **2009**, *1* (7), 552–556.

(31) Nørskov, J. K.; Rossmeisl, J.; Logadottir, A.; Lindqvist, L.; Kitchin, J. R.; Bligaard, T.; Jónsson, H. *J. Phys. Chem. B* **2004**, *108* (46), 17886–17892.

(32) Jones, L. *IOP Conf. Ser. Mater. Sci. Eng.* **2016**, *109* (1), 12008.

(33) De Backer, A.; De wael, A.; Gonnissen, J.; Van Aert, S. *Ultramicroscopy* **2015**, *151*, 46–55.

(34) Jones, L.; Yang, H.; Pennycook, T. J.; Marshall, M. S. J.; Van Aert, S.; Browning, N. D.; Castell, M. R.; Nellist, P. D. *Adv. Struct. Chem. Imaging* **2015**, *1* (1), 8.

(35) Sang, X.; LeBeau, J. M. *Ultramicroscopy* **2013**, *138C*, 28–35.

(36) De Backer, A.; Martinez, G. T.; MacArthur, K. E.; Jones, L.; Béché, A.; Nellist, P. D.; Van Aert, S. *Ultramicroscopy* **2015**, *151*, 56–61.

(37) Solliard, C.; Flueli, M. *Surf. Sci.* **1985**, *156* (PART 1), 487–494.

(38) Martinez, G. T. T.; Jones, L.; De Backer, A.; Béché, A.; Verbeeck, J.; Van Aert, S.; Nellist, P. D. D. *Ultramicroscopy* **2015**, *159* (P1), 46–58.

(39) Yu, M.; Yankovich, A. B.; Kaczmarowski, A.; Morgan, D.; Voyles, P. M. *ACS Nano* **2016**, *10* (4), 4031–4038.

(40) Sutton, A. P.; Chen, J. *Philos. Mag. Lett.* **1990**, *61* (3), 139–146.

(41) Hammer, B.; Hansen, L.; Nørskov, J. K. *Phys. Rev. B* **1999**, *59* (11), 7413–7421.

(42) Smoluchowski, R. *Phys. Rev.* **1941**, *60* (9), 661–674.

(43) Vladimirova, M.; Stengel, M.; Vita, a. De; Baldereschi, a; Böhringer, M.; Morgenstern, K.; Berndt, R.; Schneider, W.-D. *Europhys. Lett.* **2007**, *56* (2), 254–260.

(44) Ibach, H. *Surf. Sci.* **2010**, *604* (3–4), 377–385.

(45) Han, P.; Weiss, P. S. *Surf. Sci. Rep.* **2012**, *67* (2), 19–81.

(46) Calle-Vallejo, F.; Tymoczko, J.; Colic, V.; Vu, Q. H.; Pohl, M. D.; Morgenstern, K.; Loffreda, D.; Sautet, P.; Schuhmann, W.; Bandarenka, A. S. *Science (80-.).* **2015**, *350* (6257), 185–189.

(47) Gavartin, J.; Sarwar, M.; Papageorgopoulos, D.; Gunn, D.; Garcia, S.; Perlov, A.; Krzystala, A.; Ormsby, D. L.; Thompsett, D.; Goldbeck-Wood, G.; Andersen, A.; French, S. *ECS Trans.* **2009**, *25* (1), 1335–1344.

(48) Calle-Vallejo, F.; Martínez, J. I.; García-Lastra, J. M.; Sautet, P.; Loffreda, D. *Angew. Chemie Int. Ed.* **2014**, *53* (32), 8316–8319.

(49) Calle-Vallejo, F.; Loffreda, D.; Koper, M. T. M.; Sautet, P. *Nat. Chem.* **2015**, *7* (5), 403–410.

(50) Lima, F. H. B.; Zhang, J.; Shao, M. H.; Sasaki, K.; Vukmirovic, M. B.; Ticianelli, E. A.; Adzic, R. R. *J. Phys. Chem. C* **2007**, *111* (1), 404–410.

(51) Calle-Vallejo, F.; Sautet, P.; Loffreda, D. *J. Phys. Chem. Lett.* **2014**, *5* (18), 3120–3124.

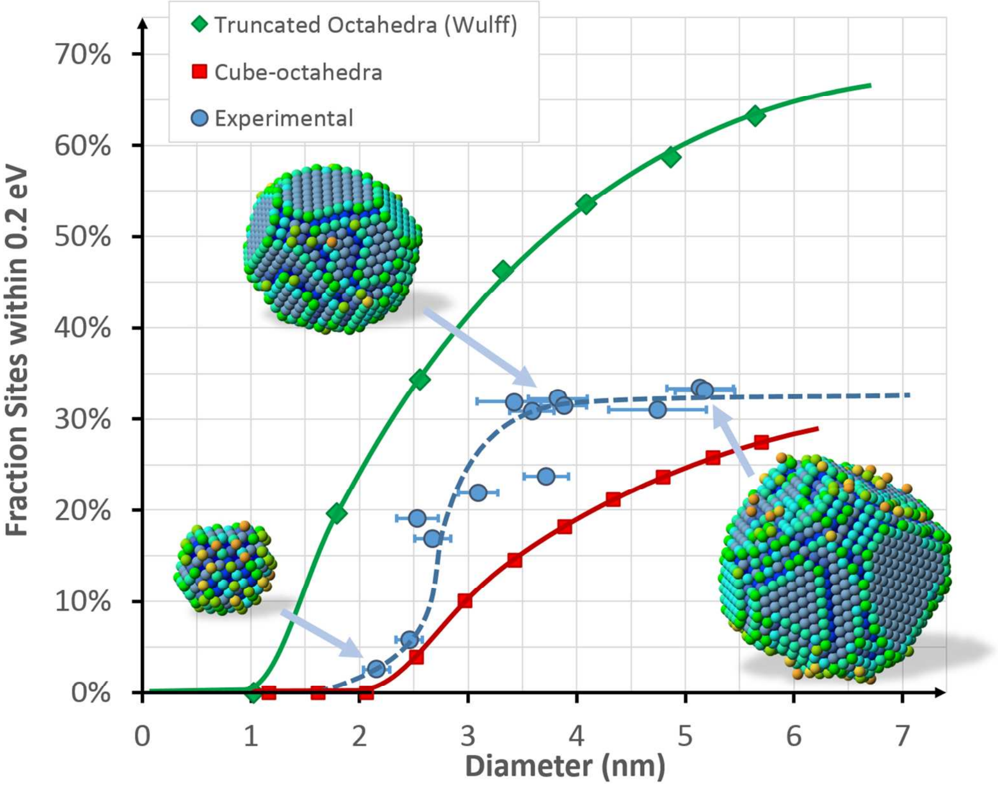

382x299mm (96 x 96 DPI)

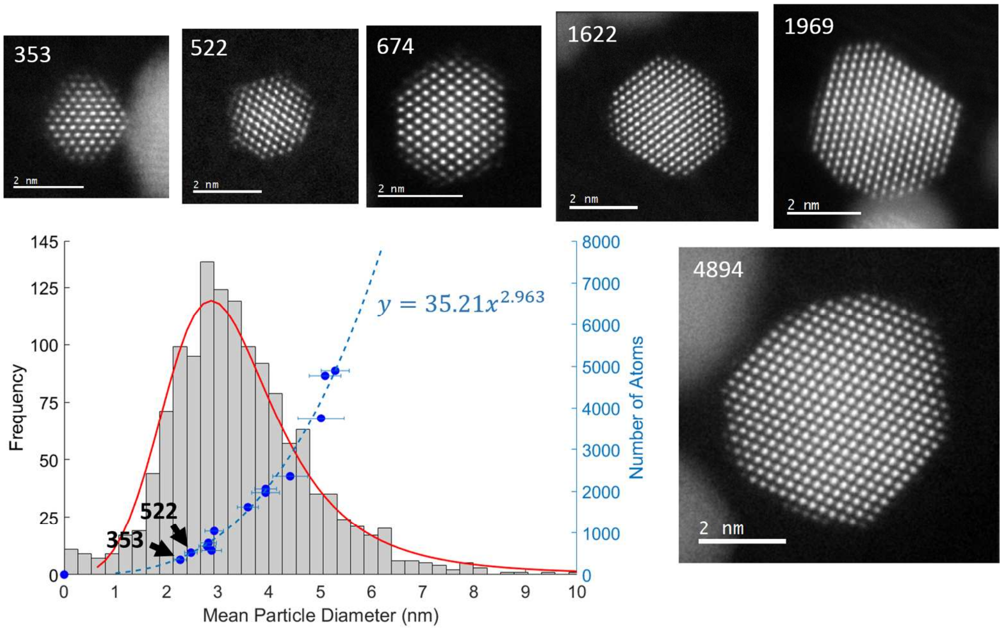

Figure 1. Particle size distribution calculated from 1342 observations (mean diameter 3.46nm, median: 3.25nm) with representative HR-STEM images labelled by total atom count. The overlaid scatter plot (blue points) shows the measured number of atoms (right axis) as a function of particle diameter. The particles with 353 and 522 atoms are shown and their relative positions in the population histogram are highlighted.

508x318mm (96 x 96 DPI)

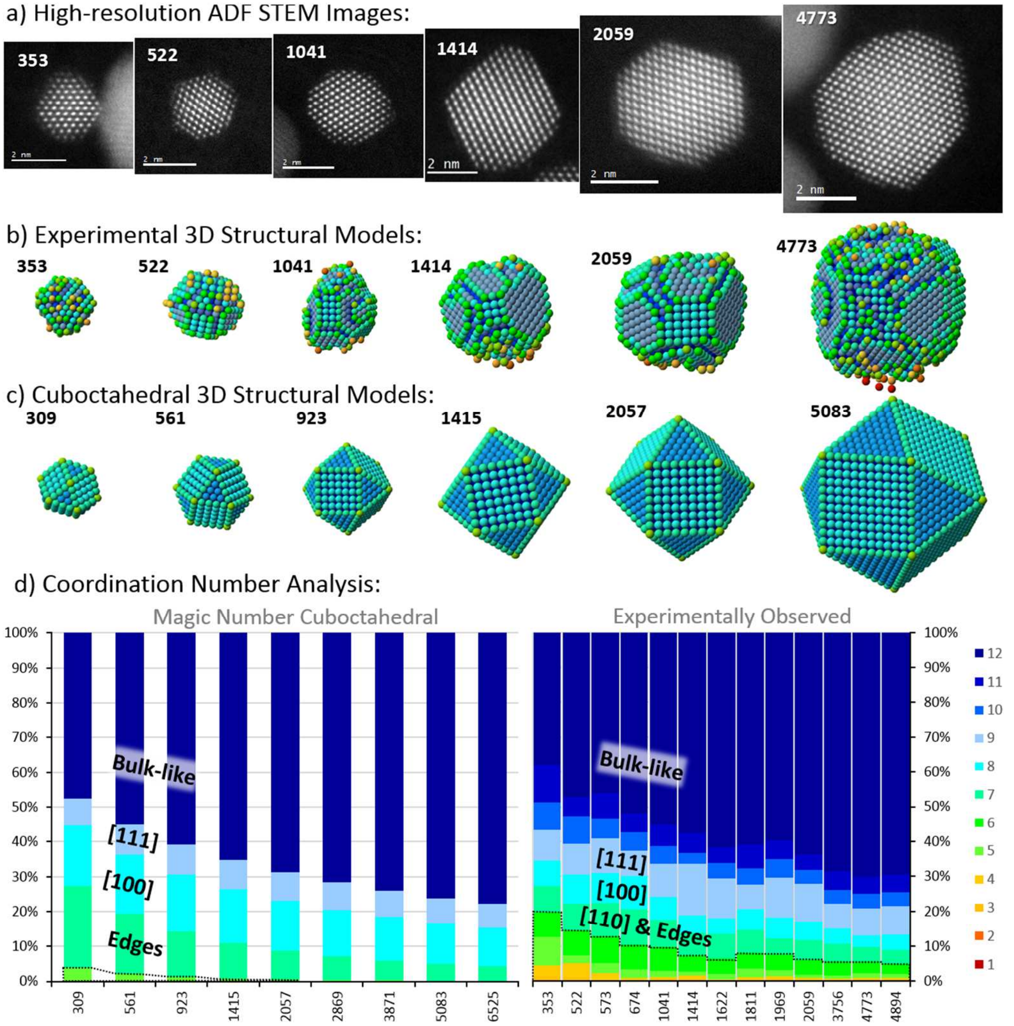

Figure 2. HR-STEM images (a) and accompanying hard-sphere models (b) for experimental particles observed with atom-counts near to magic-numbers; models are coloured by atom coordination numbers[12] and rotated to show their dominant facets. Magic number cuboctahedra are shown for comparison rotated to the same orientations (c). Population histograms (d) show the coordination number fractions as a function of particle atom-count for both magic (left) and experimentally observed particles (right). The 7, 8, and 9 coordination atoms corresponding loosely to both (110) facets and edges between facets, and (100) and (111) surfaces respectively are labelled, as well as the 'bulk-like' atoms of ≥10 coordination. The dashed area represents the fraction of low-coordination adatom, corner and step sites.

343x351mm (96 x 96 DPI)

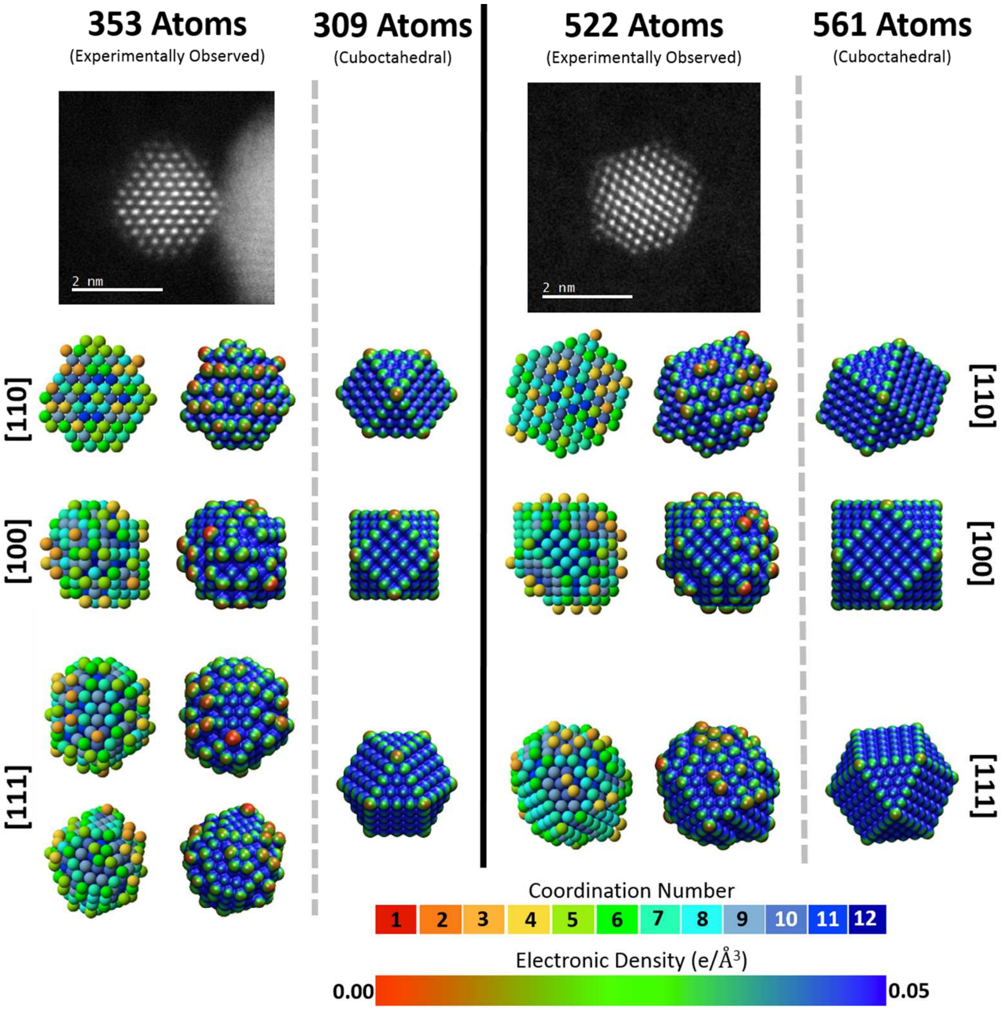

Figure 3. Coordination number and DFT analyses for the smaller (left) and larger (right) nanoparticles studied. Hard-sphere structural models were calculated from the ADF data and are coloured according to their coordination number; these are shown rotated to various viewing directions to highlight their morphology. Alongside the structural models, the DFT results showing isovalue surfaces of total electrostatic potential at 0.0 Ha colourised by the local electronic-density. Size analogue cuboctahedra DFT results are shown for comparison.

341x342mm (96 x 96 DPI)

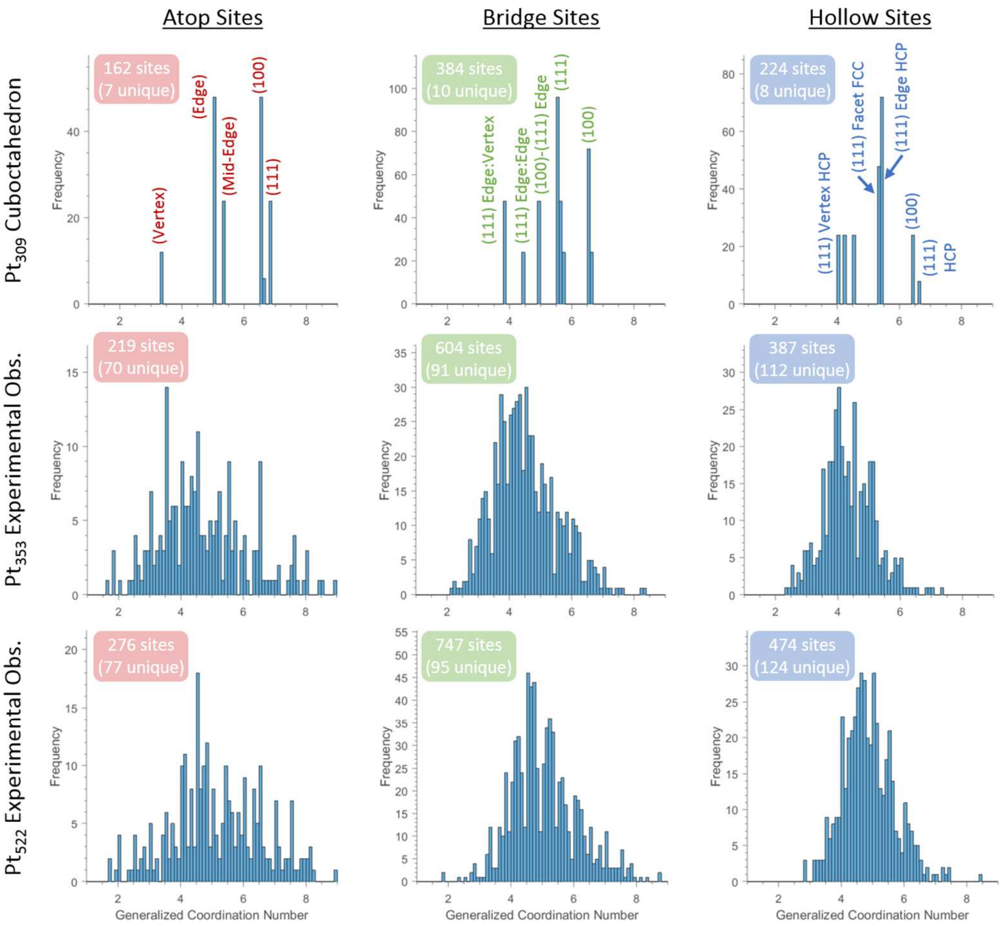

Figure 4. Histograms of the generalized coordination numbers of all possible surface atop, bridge and hollow oxygen binding sites, for the cuboctahedral Pt_{309} and the experimental Pt_{353} and Pt_{522} particles. For all plots, the number of total sites are indicated and the number of unique sites.

379x346mm (96 x 96 DPI)

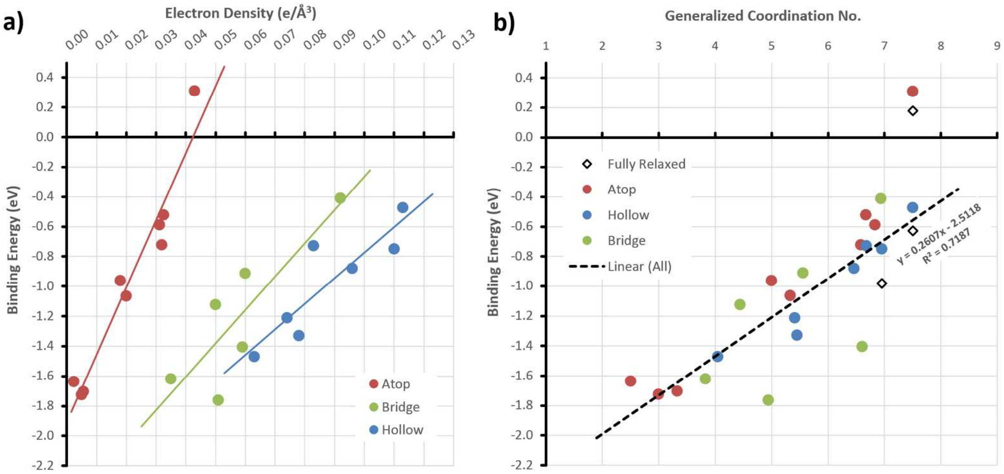

Figure 5. Calculated oxygen binding-energies for various oxygen-relaxed atop, bridge and hollow sites from both a cuboctahedral Pt_{309} nanoparticle, and from slab calculations, as a function of electron-density (a) and gCN (b). The gCN values are calculated using the formula from Calle-Vallejo et al.[48]. Black diamonds represent the results of fully-relaxed (oxygen and platinum) calculations.

581x274mm (96 x 96 DPI)

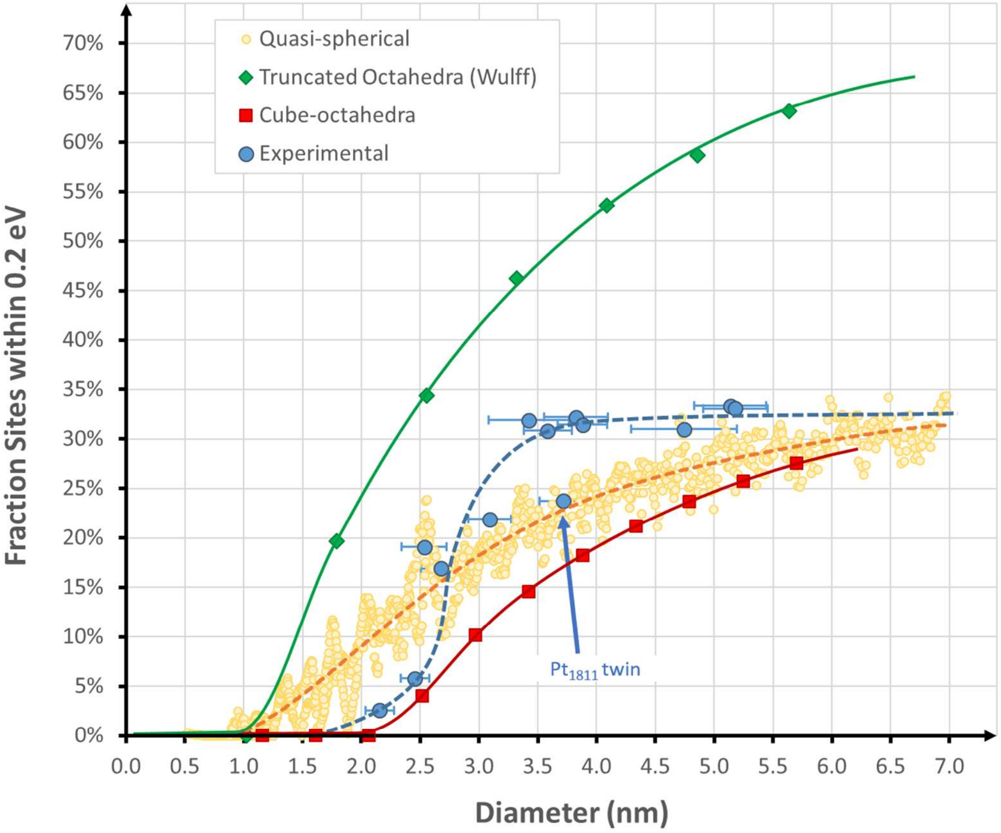

Figure 6. Fraction of surface sites within 0.2eV of optimal binding ($F_{\Delta<0.2eV}$) for the 13 experimentally observed particles, and truncated-octahedra, cube-octahedra and quasi-spherical reference particles.

352x293mm (96 x 96 DPI)